Title

Flow stress, strain hardening rate, and dislocation avalanches: Size and strain rate dependence in nano- and micro-scaled single crystal Tungsten

Author

Jiang, Katherine

Publication Date

2019

Peer reviewed|Thesis/dissertation

UNIVERSITY OF CALIFORNIA

Los Angeles

Flow stress, strain hardening rate, and dislocation avalanches: Size and strain rate dependence in nano- and micro-scaled single crystal Tungsten

A thesis submitted in partial satisfaction

of the requirements for the degree Master of Science

in Materials Science and Engineering

by

Katherine Jiang

2019

ABSTRACT OF THE THESIS

Flow stress, strain hardening rate, and dislocation avalanches:

Size and strain rate dependence in nano- and micro-scaled single crystal Tungsten

by

Katherine Jiang

Master of Science in Materials Science and Engineering

University of California, Los Angeles, 2019

Professor Vijay Gupta, Chair

The plastic behavior of body centered cubic metals generally exhibits strong strain rate and size dependence, attributed to the mobility of dislocations and availability of dislocation sources. Through in situ scanning electron microscope nano-compression testing on room temperature Tungsten single crystal micro- and nano- pillars with diameters ranging from 2000 nm to 100 nm, this work demonstrates the coupled effect of size and strain rate on plastic flow behavior. It is found that strain rate sensitivity of flow stress decreases with decreasing size, with 100 nm pillars showing negative strain rate sensitivity. Accordingly, the size effect decreases with increasing strain rate. In addition, the strain hardening rate demonstrates strong size dependence and statistically insignificant strain rate dependence, increasing with more scatter at different strain

rate as size decreases. We further show the influence of size and strain rate on pillar morphology, where smaller pillars and lower strain rates are dominated by localized plastic deformation.

The thesis of Katherine Jiang is approved.

Jenn-Ming Yang

Jaime Marian

Vijay Gupta, Committee Chair

University of California, Los Angeles,

2019

Table of Contents

List of Figures and Tables

Acknowledgments

I am grateful to my advisor Jenn-Ming Yang and my PI Vijay Gupta for allowing me the opportunity to work on this project and their patience with me. I am grateful again to Professors Jenn-Ming Yang and Vijay Gupta as well as to Professor Jaime Marian for being part of my committee. I am grateful for the guidance and understanding provided by Marta Pozuelo over the course of my time at UCLA.

Chapter 1, 3 and Sections 4.3 – 4.5 are a version of my work for a paper in preparation for publication titled Strain rate dependent flow stress, strain hardening rate, and dislocation avalanches in nano-scaled and micro-scaled Tungsten. This paper is co-authored with Pratyush Srivastava, Yinan Cui, Vijay Gupta and Nasr Ghoniem. The research presented in this paper is based on work supported by the National Science Foundation, Grant Number CMMI-1727740.

I thank Jacob Stremfel, Noah Bodzin, and Dr. Marta Pozuelo for their instruction in sample fabrication and compression technique. I also thank Pratyush Srivastava for assisting me with data visualization in addition to Dr. Yinan Cui and Professor Nasr Ghoniem for their direction and insight.

Finally, I would like to thank my family and friends.

1 Introduction

Screw dislocations in body centered cubic (BCC) metals, unlike face centered cubic (FCC) metals, have a non-planar core structure resulting in cross-slipping of screw dislocations. In BCC, slip occurs in closed packed <111> directions on different {110} planes or combinations of {110} and {112}, or {123} planes, etc., as favored by the applied stress instead of the direction favored by the critically resolved shear stress, leading to often wavy and ill-defined slip lines (Hull and Bacon, 2011). As a result, the mobility of the screw dislocation is reduced and the Peierls stress is increased. Thus, the movement of screw dislocations are much slower than edge dislocations, becoming the rate-limiting process for dislocation movement and dominating plastic deformation. Increasing flow stress due to increase in Peierls stress with increasing strain rate therefore results in the strong strain rate sensitivity found in typical BCC metals [1], [2].

It is known that submicron pillars of BCC crystals show a sharp increase of flow stress with decrease in sample size. Additionally, the stress-strain curve exhibits discrete strain bursts rather than smooth plastic flow characteristic of the bulk [3–5]. Dislocation Dynamics models have studied the underlying mechanisms that reduce this size effect and strain burst behavior; and annealing [4–8], surface orientation [9] and hydrogen embrittlement [10] have also been considered in these studies for further insight. However, most studies have been carried out at room temperature, only considering size effect on flow stress of BCC metals. In addition, models of submicron pillar experiments utilize strain rates 3 to 4 orders of magnitude higher than experimental strain rates [11]. As such, compared to the more studied size effect, there is insufficient experimental knowledge regarding the strain rate dependence of the flow stress at small scale.

1.1 Motivation of Present Study

There are few studies done on whether the strain rate will have the same strong influence on flow stress in small volumes as in the case of bulk BCC metals. At small scales, it is easy for screw dislocations to glide out of the free surface, which violates the condition that a large number of screw dislocations are stored inside the BCC crystal. In addition, the high flow stress due to size effect helps the screw dislocation to overcome the high Peierls stress. This finding of size dependent screw dislocation behavior leads to the hypothesis that the strain rate sensitivity in W may be also size dependent.

It has been found that strain rate sensitivity of BCC metals decreases with reduction in grain size for ultrafine or nanocrystalline grains [12–17]. They attribute this result to the increase in density of mixed and edge dislocations and decrease in screw dislocation density with decreasing grain size, thereby reducing strain rate sensitivity. However, a majority of these studies are done using polycrystalline materials. Huang *et al*. [12] as well as Schneider *et al*. [18] have studied the strain rate sensitivity, m, of single crystal BCC metals, in iron and molybdenum respectively. While Huang *et al*. found a tenfold reduction in m from reducing sample size from 1000 nm to 200 nm, Schneider *et al*. report strain rate sensitivity of submicron Mo pillars as similar to the bulk.

1.2 Objectives of Present Study

The intentions of this study are to answer the following: Is there a size dependent trend of strain rate sensitivity to be observed in single crystal nano- and micron-scaled W? Is there a critical size for strain rate insensitivity?

1.3 Document Organization

This paper is organized as follows: Section 2 provides background introducing tungsten, defines terminology with respect to our analysis, and the instruments used throughout our experiment. Section 3 describes sample preparation via focused ion beam and in-situ nano-compression methodology. Section 4 contains a qualitative look at various stress strain curves and analyzes the strain rate sensitivity along with discussing its size dependence as is expected from the hypothesis, among other strain rate dependent properties. Conclusions from this study as well as future work are in Section 5.

2 Background

2.1 Tungsten

Tungsten (W) has long been of great interest because of its high melting point, low sputtering rate, good corrosion resistance etc. It is widely used in high-temperature applications, such as light bulbs, cathode-ray tube, plasma-facing component and rocket engine nozzles. Under their long-term service, the experienced strain rate ranges from the creep strain rate (about 10^{-6} s^{-1}) to very high strain rate (about 10^{6} s^{-1}). As a typical body centered cubic (BCC) metal, the plastic behavior of W generally exhibits strong strain rate sensitivity. Therefore, understanding the deformation process with respect to the strain rate effect under the scope of the size effect is important for insight to be considered in the design of the W component.

2.2 Flow Stress

The yield strength of a metal deformed in uniaxial condition is often interchangeably referred to as the flow stress [19], defined theoretically as the stress applied to cause a material to continue to

deform or ‘flow’ in its plastic range. While yield strength of bulk material is estimated as the stress at 0.2% offset strain, the flow stress at micron- and nano-scale is quantitatively measured at strain value between 2% and 10% [3]. This is to avoid the effect of initial microplasticity and misalignment prior to the elastic region of the stress-strain curve. In this study, engineering stress at 8% engineering strain is treated as flow stress (also referred to as yield strength). It is also of note that all stress values in this paper are values for compression, which can not be assumed to be the same as those in tension.

2.3 Strain Rate Sensitivity, m

The strain rate sensitivity parameter, m, is defined as

$$m = \frac{\partial \ln \sigma_y}{\partial \ln \dot{\varepsilon}} \tag{2.1}$$

where σ_y is the yield strength and $\dot{\varepsilon}$ is the applied strain rate. Parameter m is thus the slope of the experimental data in log-log plot, where m = 0 is considered strain rate insensitive.

2.4 Strain Burst Events

Unlike bulk materials with smooth, continuous stress strain curves, nano- and micro-scale materials exhibit intermittent flow in the plastic region. These strain bursts enabled by dislocation avalanches are attributed to rapid movement of dislocations when internal strain exceeds the applied strain rate [20], manifested as a rapid increase in strain over relatively stable stress followed by a rapid drop in the stress signal (stress relaxation) in stress-strain curves during strain (displacement) controlled loading mode. For clarity, specifically the rapid increase in strain will be denoted as ‘strain burst,’ followed by a stress drop and reloading. These three segments make up one ‘strain burst event.’

2.5 Scanning Electron Microscopy

As this work requires the mechanical testing of micron and nano-sized samples, scanning electron microscopy (SEM) is an important tool for both sample creation and characterization. An electron beam is scanned across the sample, upon which electron-sample interactions produce various emissions including characteristic x-rays, secondary electrons, backscattered electrons, etc. For the purpose of this study, the secondary electron emission provides sample morphology and topography of the sample. These electrons are collected by detectors and digitized into a 2D electron micrograph, updated as the beam scans across the desired area.

2.6 Focused Ion Beam Milling

Focused ion beam (FIB) is used as a fabrication method for the samples of this study. FIB works similarly to SEM but rather than an electron beam, uses an ion (typically gallium Ga^+ ions) beam to scan the area. As opposed to the non-destructive interaction of low-mass electrons, because even the lightest ions are 2000 times the mass of an electron (gallium being about 5 orders of magnitude greater than electron mass), scanning with ions is typically destructive to the surface. This means the focused ion beam can be aimed to modify the specimen surface, controlled with nanometer scale precision. The milling of the surface is controlled by several variables, including accelerating voltage, current, and exposure region and time.

A dual-beam system, where the electron and ion beams intersect at a 52° angle at the sample surface, combines the benefits of both electron and ion beams. The SEM component is typically used to monitor and guide the FIB milling of the surface via sample navigation and immediate imaging during the milling process.

2.7 Hysitron Nanoindentation System

A specialized nano-compression set up was necessary to mechanically characterize the samples in this study, as macroscopic systems would not be sufficient for the size and sensitivity required. The Hysitron PI 85 SEM PicoIndenter used in this study interfaces as an attachment in the SEM to perform nanomechanical testing with real-time imaging, allowing positioning of the sample stage with respect to the probe with high accuracy and precision as well as observing of the actual compression. Raw force, and displacement data is collected by the system, with force noise below 0.4 μN and displacement noise below 1 nm, at manually set regular time intervals.

3 Experimental Methods

3.1 Micro and Nano-pillar Sample Preparation

This study used a cylinder of high purity single crystal W (99.999%) as the bulk material from which samples were milled. The initial W sample was acquired from Goodfellow Co, with as-received dimensions of 1mm thickness and 9mm diameter, oriented (100). The sample was first polished using 600 grit and 1200 grit silicon carbide abrasive discs until smooth to the naked eye, then underwent a final polish using 1μm α-alumina powder. Samples were inspected via optical microscope for surface defects before being used to prepare pillars. Further inspection of the surface morphology was carried out via SEM using the FEI Nova 600 NanoLab DualBeam™-SEM/FIB system to choose appropriate locations for pillar milling. All pillars for in-situ compression were milled from the same bulk sample.

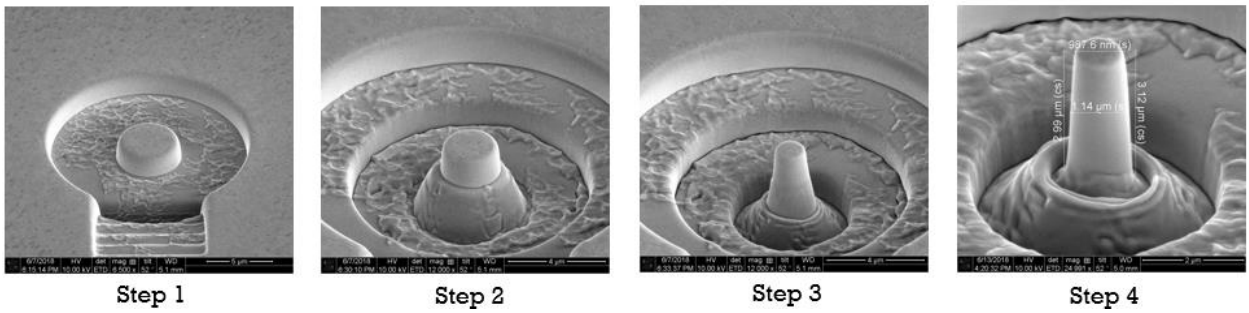

Figure 1. 4-step FIB manufacturing process demonstrated in a 1um pillar.

Pillars ranging from 100 nm to 2000 nm median diameter were manufactured via top-milling using the FIB of the Nova 600, with a gallium ion source operating at 30 kV, following Pozuelo *et al*. [21]. The multiple-step pillar milling procedure first begins with creation of the base well and viewing window for clearance of the compression tip and line of sight for alignment when performing in-situ nano- and micro-compression, calculated such that the pillar base is visible at a 10° tilt of the surface. This first step was performed at currents ranging from 0.5 nA to 5 nA, dependent on final pillar diameter. The following steps to shape the pillar were carried out at increasingly lower currents to reduce the ion damage to the final pillar. These intermediate steps both reduce pillar diameter to the desired size as well as increase well depth. A final cleaning step to reduce taper was implemented at extremely low currents after all intermediate steps were completed, ranging from 1 pA for the smallest (100 nm) pillars to 100 pA for the micropillars.

Final pillars maintained a taper angle of (2.03 ± 0.56)°, (2.18 ± 0.38)°, (2.71 ± 0.54)°, (3.91 ± 0.81)°, (3.39 ± 0.75)° for 2 µm, 1 µm, 500 nm, 200 nm, and 100 nm pillars, respectively. As an effect of minimizing taper and still reaching 100 nm diameter, the smallest pillars were elongated to a 1:5 aspect ratio (diameter : height) from extended cleaning steps, whereas all other pillar sizes maintained an aspect ratio of approximately 1:3, as is common [18], [22], [23] for mechanical testing of micropillars.

3.2 In-situ Nano-compression

The Hysitron PI 85 SEM PicoIndenter equipped with a flat punch tip of 5 um diameter was used for in-situ compression. The sample is mounted to the PI 85 using colloidal silver paint rather than carbon tape to prevent compliance during compression. The SEM stage is tilted 10° to allow viewing of the sample surface and sub-surface pillar location.

Alignment for compression was performed manually and aided by SEM, first through moving the sample stage of the PI 85 vertically such that the punch tip is directly to the side of the pillar (Figure 2a), and then horizontally. A final approach to raise the sample stage (holding the pillar) towards the probe is done before starting the loading curve. All final alignments are done with 10nm steps to ensure uniaxial load with pillar placed directly center under the flat punch tip. All tests were performed at room temperature.

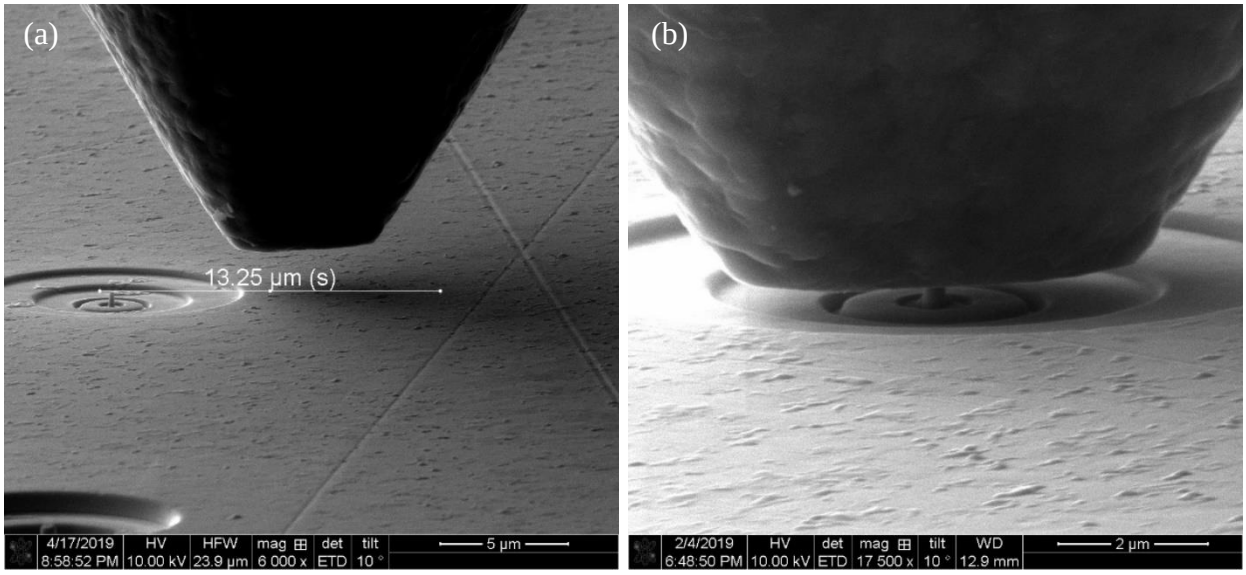

Figure 2. Centering of flat punch tip to 200 nm pillar for uniaxial load (a) vertically (b) horizontally and final approach.

Loading was performed under displacement control to achieve desired strain rates ranging from 10^{-3} s^{-1} to 10^{-1} s^{-1}. Data acquisition rate per experiment were chosen dependent on pillar dimension and compression speed.

Diameter	100 nm	200 nm	500 nm	1 um	2 um
Length	500 nm	600 nm	1.5 um	3 um	6 um
Strain Rates	Displacement rate of the compressor tip				
10^{-3} s^{-1}	0.5 nm/s	0.6 nm/s	1.5 nm/s	3 nm/s	6 nm/s
10^{-2} s^{-1}	5 nm/s	6 nm/s	15 nm/s	30 nm/s	60 nm/s
10^{-1} s^{-1}	50 nm/s	60 nm/s	150 nm/s	300 nm/s	600 nm/s

Table 1. Strain rate parameters for various sizes.

Initial compressions were for very high strain but eventually due to occurrences of strain burst and large physical deformation of the pillar, maximum strain was limited to smaller values.

3.3 Sample Imaging

Samples were imaged under electron beam using the SEM mentioned in Section 2.5 before, during, and after compression. Scanning electron micrographs were taken before compression to measure pillar dimension for stress-strain calculations, as described by Section 4.2, with a 52° tilt from perpendicular milling of the ion beam. During compression, the scanning electron microscope provided ‘live’ imaging focused on the flat punch tip at the maximum allowable tilt for the Hysitron PI 85 system, 10°. Post-compression pillars have images also taken at 52° for comparison against their undeformed versions, with rotational angles set such that slips occurred during compression are shown (emphasized with dashed line on Figure 3b).

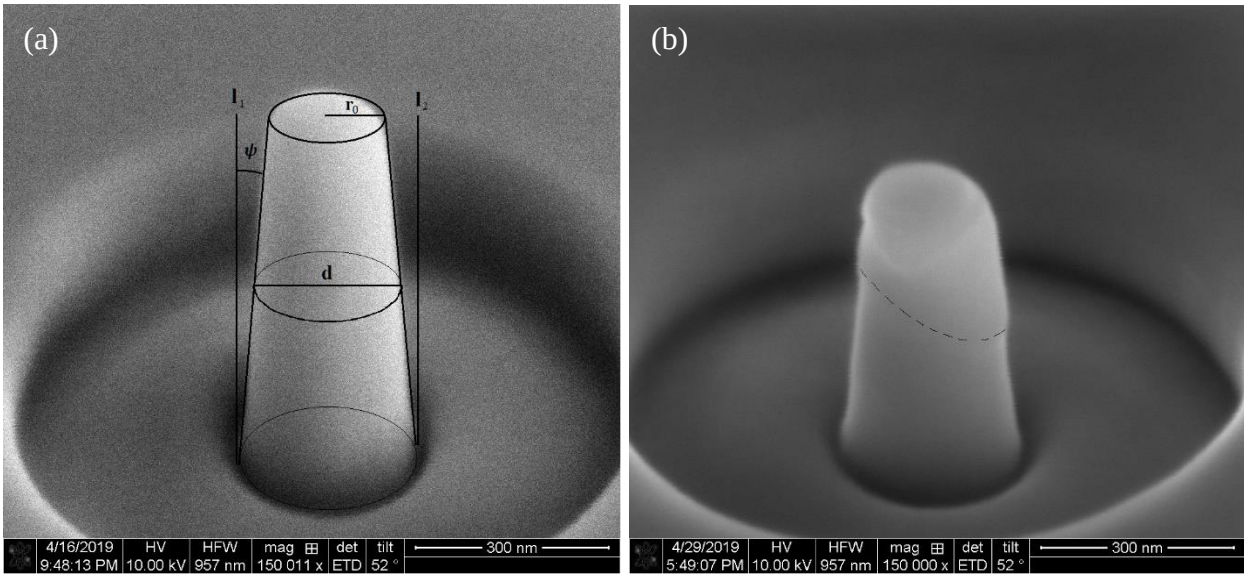

Figure 3. SEM images of 200 nm pillar after (a) milling (b) compression.

4 Results and Discussion

4.1 Effects of FIB Sample Fabrication

It is well known that FIB milling can introduce surface defects to the milled pillars. As the relative surface area to volume ratio increases with decreasing pillar size, these effects become more noticeable. FIB-prepared copper micropillars have been shown to have broad variation of initial stiffness of the material, or a smaller loading curve slope [24] [25]. Shan *et al*. [26] also find that samples of d < 200 nm have FIB irradiation defects progressively leave the pillar upon loading for Ni crystals. These effects can therefore be circumvented by selecting flow stress values at later strain $\varepsilon > 2.5\%$ [25], as is done in this study.

The effect of taper should also be noted for the following sections. It is known that tapered sample geometry results in inhomogeneous deformation, with higher applied stress experienced at the top of the sample where the cross-sectional area is smaller [3]. This results in an artificial increase in strain hardening rate as compared to taper-free samples. Shan *et al*. [26] report a change in pillar

morphology after initial compression from 4.5° taper to taper-free, while Zhang *et al.* [25] account for taper effect for their stress-strain calculations only in the elastic modulus:

$$\frac{E_{\text{measured}}}{E_{\text{true}}} = 1 + \frac{L_0}{r_0}\tan\psi \tag{4.1}$$

where $L_0 = \frac{l_1+l_2}{2}$ is initial average pillar height and r_0 is radius at the top of the pillar. Thus, one can again assume that taking flow stress values and strain hardening rate at later strain will mitigate the taper effect on our data.

4.2 Stress-Strain Curves

Stress-strain curves were calculated from raw force-displacement data obtained by the Hysitron PI 85. Due to the 10° tilt for alignment, the flat punch tip covers the pillar in the SEM view during compression (Figure 2b). Thus, dynamic pillar dimensions during deformation for the calculation of true stress and true strain were unavailable. As a result, engineering stress-strain curves are used for this study, where initial length of the pillar is L_0, and cross-sectional area is calculated from the diameter, d, at the mid-point of the pillar as labeled in Figure 3a. Select engineering stress-strain curves are presented in the following.

4.2.1 Strain Rate Comparison of Stress-Strain by Sample Size

A qualitative look at stress-strain curves organized by sample size is presented in this section.

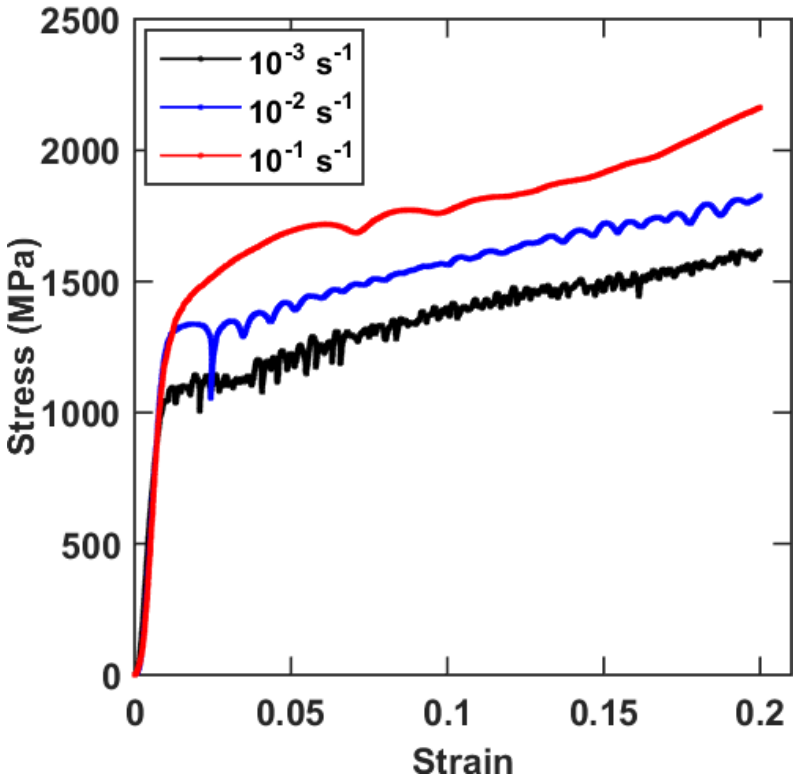

Figure 4. Engineering stress-strain curve for 2000 nm pillar.

At 2000 nm pillar diameter, the stress-strain curve exhibits obvious strain rate effect; there is an increase of approximately 250 MPa for each magnitude of strain rate. There is little to no overlap past the elastic region of the curves: each curve is very distinct. The 10^{-1} s^{-1} stress strain curve of Figure 5 exhibits smooth and mostly increasing plastic region, similar to bulk stress strain curves. As the strain rate increases, the instability of the plastic region increases, with 10^{-3} s^{-1} showing the shortest difference in strain before another stress drop (dislocation avalanche) occurs. However, all stress-strain curves remain relatively smooth despite the fluctuations in stress.

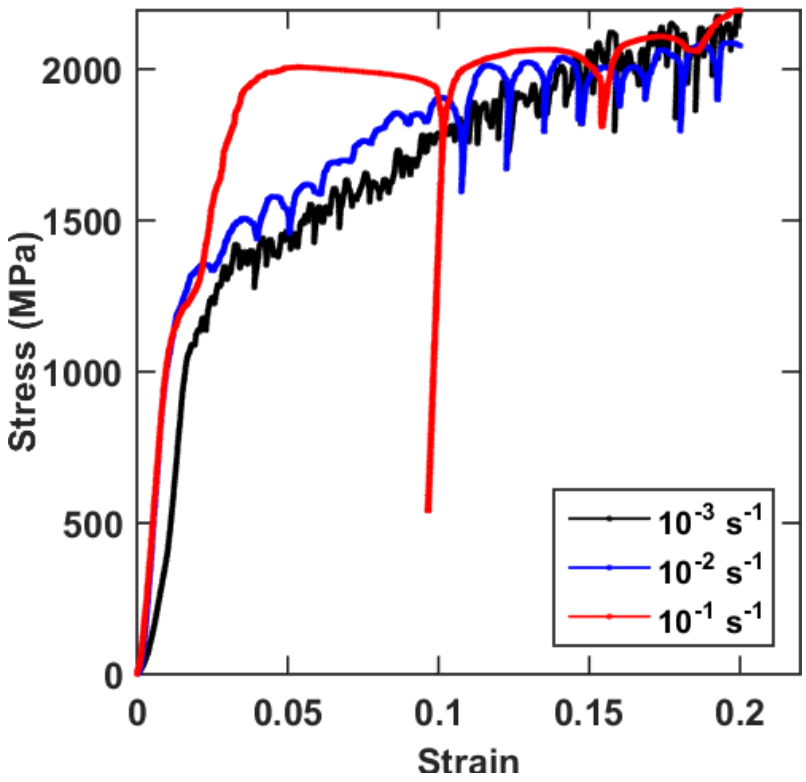

Figure 5. Engineering stress-strain curve for 1000 nm pillar.

As pillar diameter is reduced to 1000 nm, the stress-strain curves become less distinct with occasional overlaps at later strain. However, for the consideration of flow stress at less than 0.1 strain, the strain rate effect still applies. All curves now exhibit unstable plastic behavior, but as in 2000 nm, the 10^{-1} s^{-1} stress strain curve remains the smoothest and the 10^{-3} s^{-1} the most frequent in strain with respect to strain burst events.

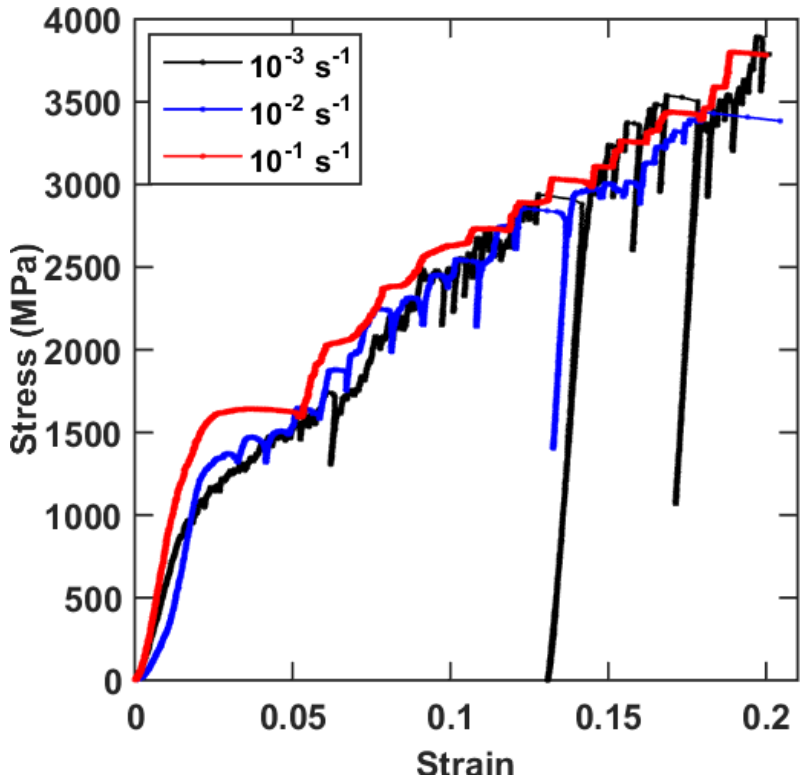

Figure 6. Engineering stress-strain curve for 500 nm pillar.

At 500 nm, the stress-strain curves exhibit frequent overlap. While the flow stress initially shows distinct strain rate sensitivity, the large strain burst of the 10^{-1} s^{-1} stress-strain curve reduces the difference in flow stress between all three strain rates. In contrast to the rounded features present in Figures 5 and 6, the shape of the plastic flow now appears to exhibit distinct strain burst and stress relaxation sections: a stretch of relatively stable stress as strain increases, then a catastrophic drop in stress followed by reloading. This change is also evident when comparing the shape of each strain burst event in the stress-strain plot in Figures 6 and 7 at low strain and high strain, where the high strain events show more angular features.

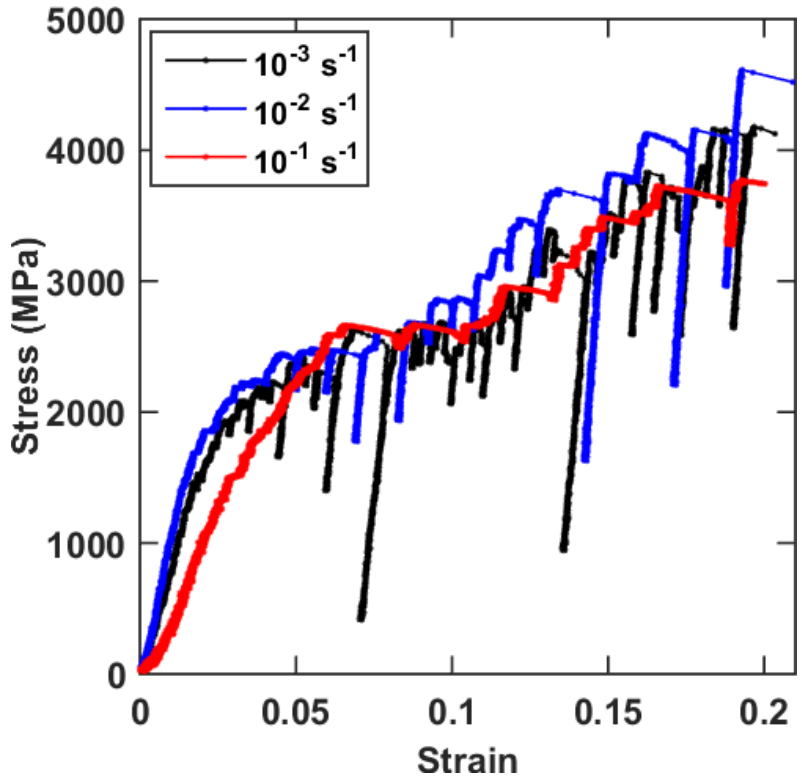

Figure 7. Engineering stress-strain curve for 200 nm pillar.

From 500 nm to 200 nm, while the reloading sections for 500 nm follow the slope of the initial elastic region, these sections have higher slope than the initial elastic region in 200 nm and 100 nm stress-strain curves. This will be further addressed in Section 4.2.2. The strain burst following each reloading curve also demonstrates a more pronounced decrease in stress as strain increases for 200 and 100 nm compared to d > 500 nm. The slope of this linearly decreasing stress is the same for all curves regardless of strain at given pillar sizes, with 100 nm pillar having larger absolute slope than 200 nm.

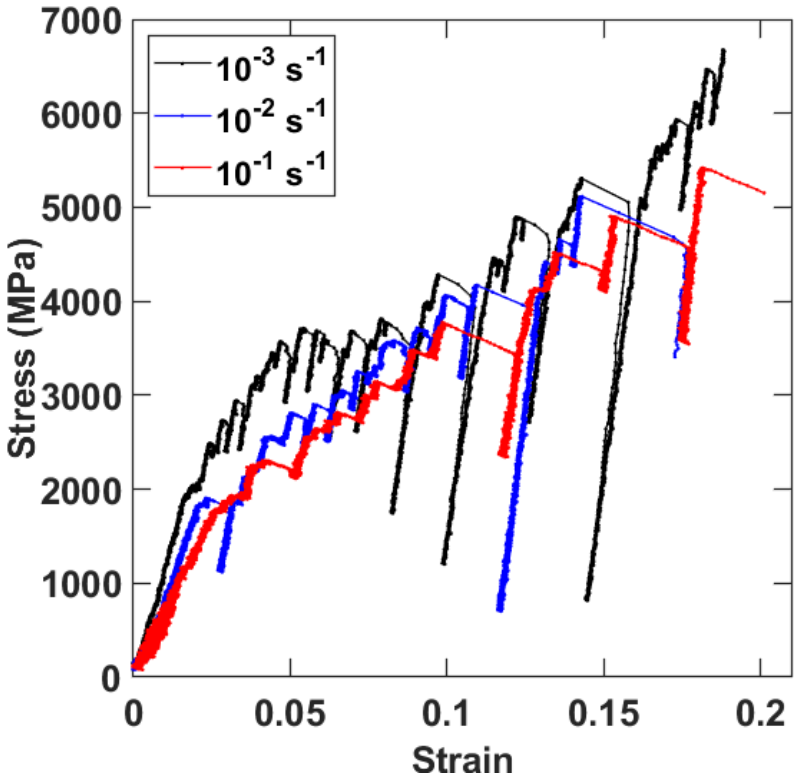

Figure 8. Engineering stress-strain curve for 100 nm pillar.

Further decreasing to 100 nm pillar diameter, 10^{-3} s^{-1} shows generally highest stress at all strains compared to other strain rates. However, as in the 500 and 200 nm pillars, there is overlap of the stress-strain curves due to frequent strain bursts, reducing the differences in flow stress across strain rates.

As with previous pillar diameters, these strain burst events are more frequent in strain at lower strain rate. The distinct sections of the strain bursts are also more evident than those of the larger pillar sizes. There is also a general trend evident in the above figures where a larger period in strain of stable stress is associated with a more drastic stress drop following.

4.2.2 Size Comparison Stress-Strain by Strain Rate

A qualitative look at stress-strain curves organized by strain rate is presented in this section.

These stress strain curves demonstrate, as expected, the size effect. Regardless of strain rate, each set of stress-strain curves demonstrates higher stress at smaller pillar diameter.

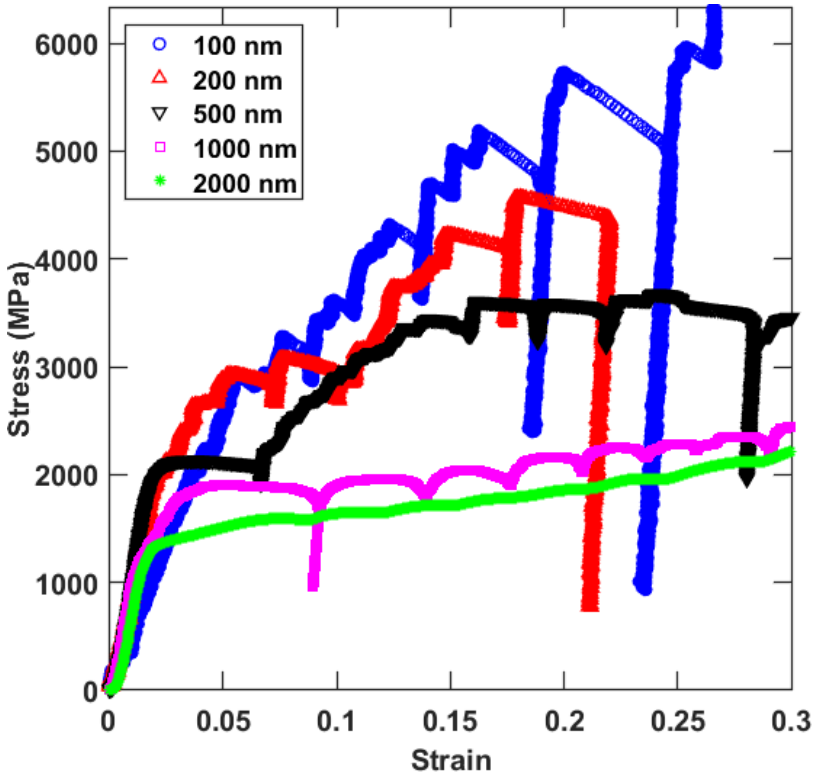

Figure 9. Engineering stress-strain curve for 10^{-1} s^{-1} strain rate.

From the curves of various pillar diameters at strain rate of 10^{-1} s^{-1}, the increasing magnitude (stress drop) and frequency (in strain) of strain burst event as mentioned in Section 4.2.1 becomes evident. Also visible is the transition from smooth to distinct strain bursts with decreasing pillar diameter as well as the increasing slope of the strain burst.

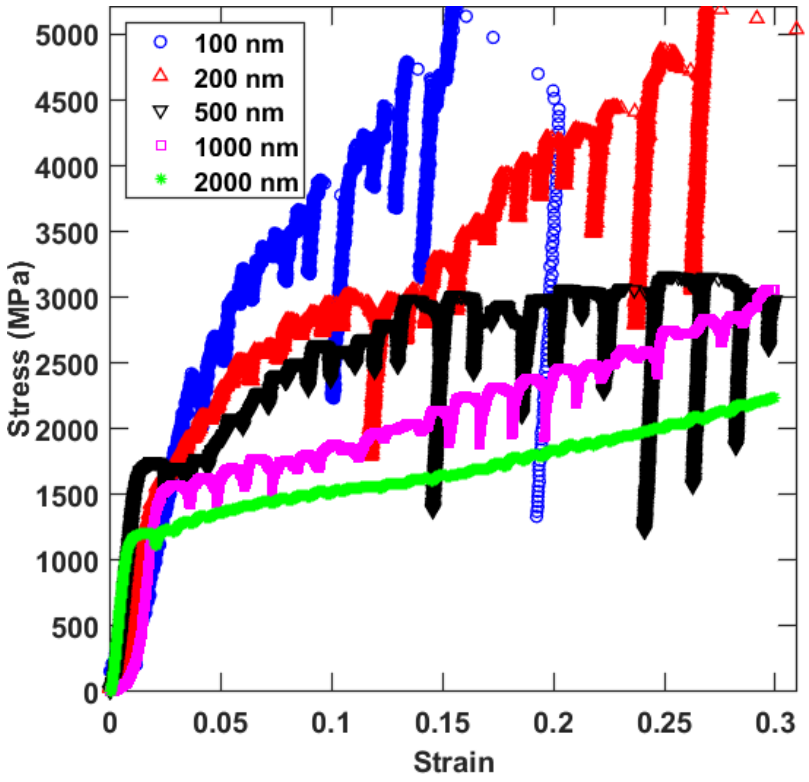

Figure 10. Engineering stress-strain curve for 10^{-2} s^{-1} strain rate.

Like in Figure 9, the strain burst becomes more distinct and increases in slope with decreasing diameter. Interestingly, for the strain burst events at 10^{-2} s^{-1} strain rate, the strain burst magnitude (strain burst event frequency) does not appear to increase as pillar diameter decreases, while the stress drop magnitude does. This same trend is observed for pillars compressed at 10^{-3} s^{-1}.

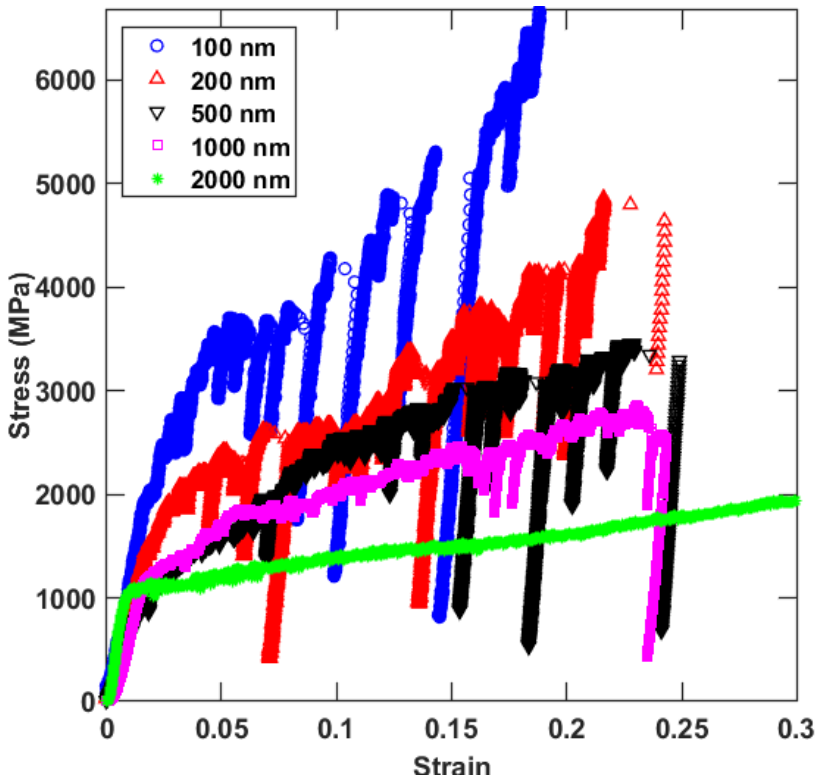

Figure 11. Engineering stress-strain curve for 10^{-3} s^{-1} strain rate.

From Figures 9 through 11, the reloading step of each strain burst generally follows the slope of the elastic region. However, this is not always the case, especially for the 100 nm diameter pillars where the reloading slope is the same as all other pillar sizes, but their elastic region is lower in slope. Considering that elastic constants are known to be independent of scale, this initial reduction of slope may be attributed to surface effects occurring in the original elastic region becoming more significant at smaller pillar diameter, such as FIB damage as mentioned in Section 4.1. The large variation in elastic modulus may also be explained from Equation 4.1, where the taper of sample pillars can result in E_{measured} ranging from 1.2 to 1.6 times E_{true}. The parallel slopes of the reloading curves across all sizes then supports the assumption that FIB damage and taper effects are mitigated at later strains.

4.3 Flow Stress Behavior

A quantitative analysis of the stress-strain curves with respect to flow stress, strain rate sensitivity, and size is presented in this section. As mentioned in Section 2.2, flow stress values were measured at 8% engineering strain.

4.3.1 Strain Rate Dependence of Flow Stress

The values for flow stress are plotted against strain rate in log-log to find strain rate sensitivity parameter, m, defined by Equation 2.1 and shown in Figure 12 as the slope of each set of data.

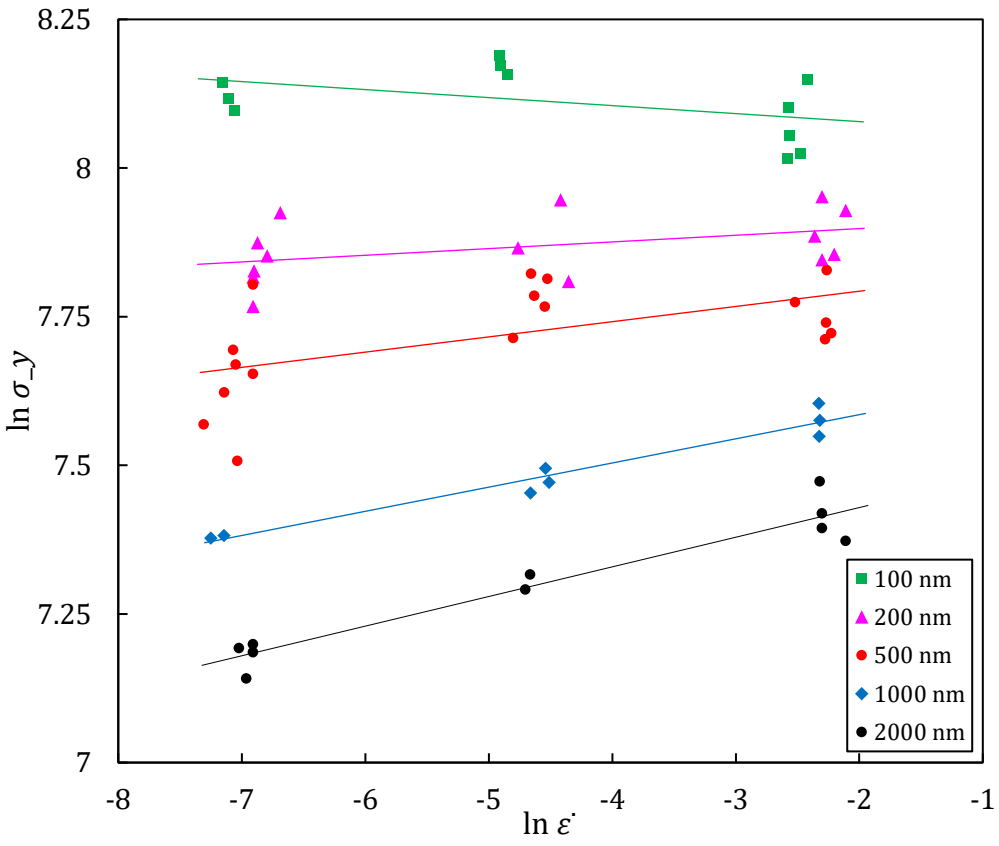

Figure 12. Strain rate sensitivity of flow stress for micro- and nano-pillars. Parameter m for 100 nm to 2000 nm respectively are (-0.013 ± 0.009), (0.011 ± 0.007), (0.026 ± 0.009), (0.041 ± 0.004), and (0.050 ± 0.005).

Despite the scatter of the flow stress data, a clear trend where strain rate sensitivity decreases with decreasing pillar size is evident. The strain rate sensitivity m decreases about fivefold from 0.050 to 0.011 when pillar size is decreased from 2000 to 200 nm, with 100 nm diameter showing negative value for m. This trend is also evident if choosing flow stress at 5% strain, with m decreasing from 0.061 at 2000 nm to 0.009 at 100 nm. It can be seen from the large scatter in Figure 10 also that while strain rate sensitivity is inverted for pillars of size 100 nm, both 100 nm and 200 nm have m extremely close to 0 and can be said to be strain rate insensitive, further supported by the non-negative near zero m for 100 nm at 5% strain. It can thus be concluded that there is *size dependence of the strain rate sensitivity* for single crystal Tungsten, beginning at size scale larger than 2000 nm and becoming strain rate insensitive around 200 nm.

An attempted rationalization of the size effect on m is presented by Huang *et al*. [12] considering the contributions of lattice friction force and dislocation-obstacle interactions to flow stress:

$$\sigma(\dot{\varepsilon}) = \sigma_{\text{friction}}(\dot{\varepsilon}) + \sigma_{\text{bowout}}(\dot{\varepsilon}, L) \tag{4.2}$$

where σ_{bowout} depends on a characteristic length L between pinning points and thus sample size, while σ_{friction} depends on dislocation velocity and therefore is sensitive to strain rate. When the sample size is large, lattice friction force dominates the flow stress. As L is reduced through sample size reduction, σ becomes dominated mostly by σ_{bowout}. As the strain rate sensitivity of BCC metals is typically attributed to the increase in Peierls stress with increasing strain rate and the slow mobility of screw dislocations, the size effect helps reduce the contribution of σ_{friction} by helping with overcoming the Peierls stress barrier to improve dislocation mobility. This transition in flow stress from being lattice friction dominated to dislocation-obstacle dominated thus decreases strain rate sensitivity. In addition, the high flow stress level at nanoscale has been shown

in molecular dynamic simulation by Huang *et al*. [7] to reduce the mobility difference of screw and edge dislocations, thereby also reducing the strain rate dependence of flow stress.

A similar explanation is found through inspection of the stress-strain curves in Section 4.2. Competing effects of strain softening and strain hardening is also a known cause of reduced strain rate sensitivity, such as in Ferrite-Martensite DP980 [27], where each constituent phase either strain hardens or softens. For single crystal tungsten, the increased dislocation mobility from size effect contributes to the softening manifested in the slope of the strain burst. This high plastic strain rate strain burst is induced by mixed dislocations repeatedly breaking away from their pinning points once they are unstable under the instantaneous stress level, stopping when the moving edge part annihilates at the free surface. It is observed in Figures 7 and 8 that for a given pillar diameter, at higher strain rate the dislocation bursts are longer and less frequent in strain, consistent with the logic that at lower strain rate the high plastic strain rate of 'strain burst' is reached more easily and frequently [20]. Combined with the slope of the strain burst being the same across all strain rates, for the same pillar diameter, the higher strain rate pillar therefore has a larger decrease in stress per burst. If the stress required for strain burst, σ_{bowout}, is similar for all pillars of the same diameter, then this explanation may even justify the negative m found in 100 nm pillars at 8% strain compared to its positive m at 5%.

4.3.2 Size Dependence of Flow Stress

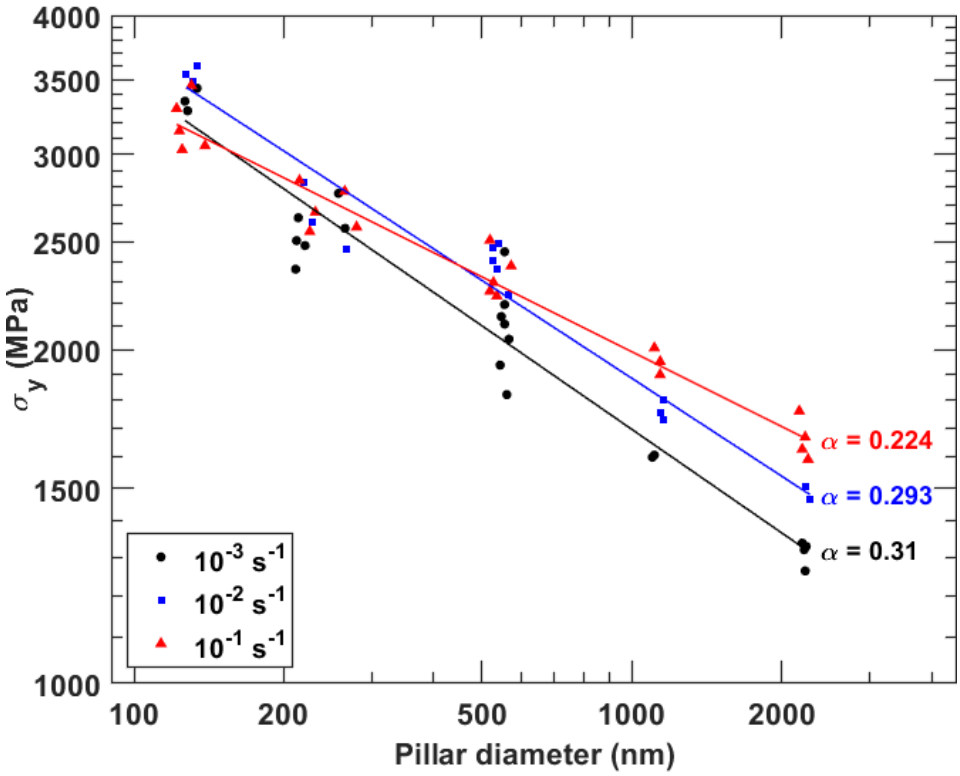

Figure 13. Size effect on flow stress for micro- and nano-pillars.

It is observed that while with reduction of sample size the flow stress increases as is expected of size effect, the flow stress data for different strain rates lessens in scatter due to the transition from strain rate sensitive at larger pillar diameter to strain rate insensitive. The competition between size effect and strain rate effect on flow stress can thus be interpreted through the strain rate dependence of size effect. From a quantitative point of view, the size effect is described by the general equation:

$$\sigma = \sigma_0 + kD^{-\alpha} \tag{4.3}$$

where σ_0 is the bulk strength of the material, D is the characteristic length scale, k is a constant, and α is the power law exponent. A larger exponent therefore corresponds to a stronger size effect: Figure 13 shows α increasing from 0.224 to 0.31 as strain rate decreases from 10^{-1} s^{-1} to 10^{-3} s^{-1}.

Thus, there is also *strain rate dependent size effect* present, with it being more significant at lower strain rate.

4.4 Strain Hardening Rate

Strain hardening rate, calculated as the slope of the stress-strain curve between 5% and 15% strain, is shown in Figure 14 as averaged data for various sample sizes at three strain rates. The strain hardening rate is expected to increase with decreasing pillar diameter as reported by previous studies on FCC and BCC metals [28], [29]. The general trend of size dependence is attributed to exhaustion of weak dislocation sources in smaller pillars leading to requirement of higher stresses to activate new dislocation sources. This depends on initial concentration of dislocation sources, which may be influenced by the ion damage caused by FIB milling process as mentioned in Section 4.1.

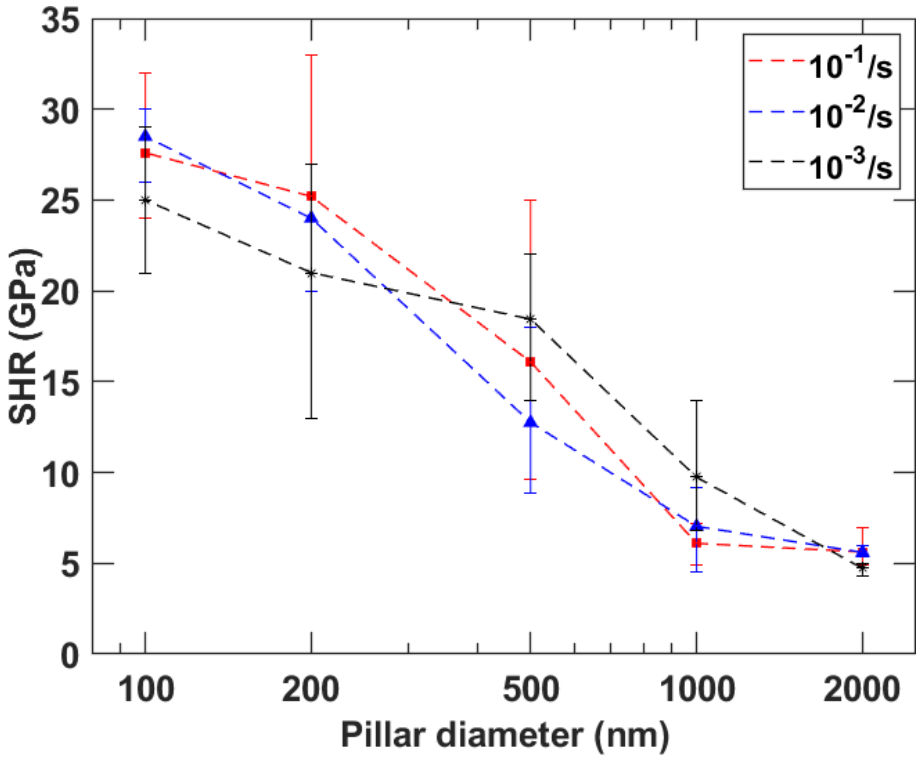

Figure 14. Size and strain rate dependence of strain hardening rate.

With respect to strain rate dependence of the strain hardening rate, it is evident that there is a large scatter of the strain hardening rate at sample sizes other than 2000 nm, enough that despite the difference in value for strain hardening rate it remains statistically indistinct. A qualitative evaluation of the strain hardening rate through Figures 4 to 8 also suggests statistically indistinct strain hardening rates, while the large scatter of strain hardening rates for d < 2000 nm coincides with the appearance of strain burst events at smaller pillar diameter.

The inversion of 10^{-1} s^{-1} from low strain hardening rate (compared to the other strain rates) at d > 500 nm to high strain hardening rate is also explained visually through strain burst events. Comparing the stress-strain curves from 1000 nm to 100 nm, one notices a decrease in strain burst magnitude – also noticeable through Figure 9. At large strain burst magnitude, strain hardening rate is artificially lowered through mostly taking the slope of the strain burst rather than the entire stress-strain curve. Thus, as pillar size decreases so that strain burst magnitude decreases and frequency increases, the strain hardening rate is no longer dominated by the slope of the strain burst and therefore increases. To a point, this effect is also evident in 10^{-2} s^{-1}, but not nearly as drastic.

4.5 Pillar Morphology

Representative pillars compressed at 20% to 25% strain are shown in Figure 15.

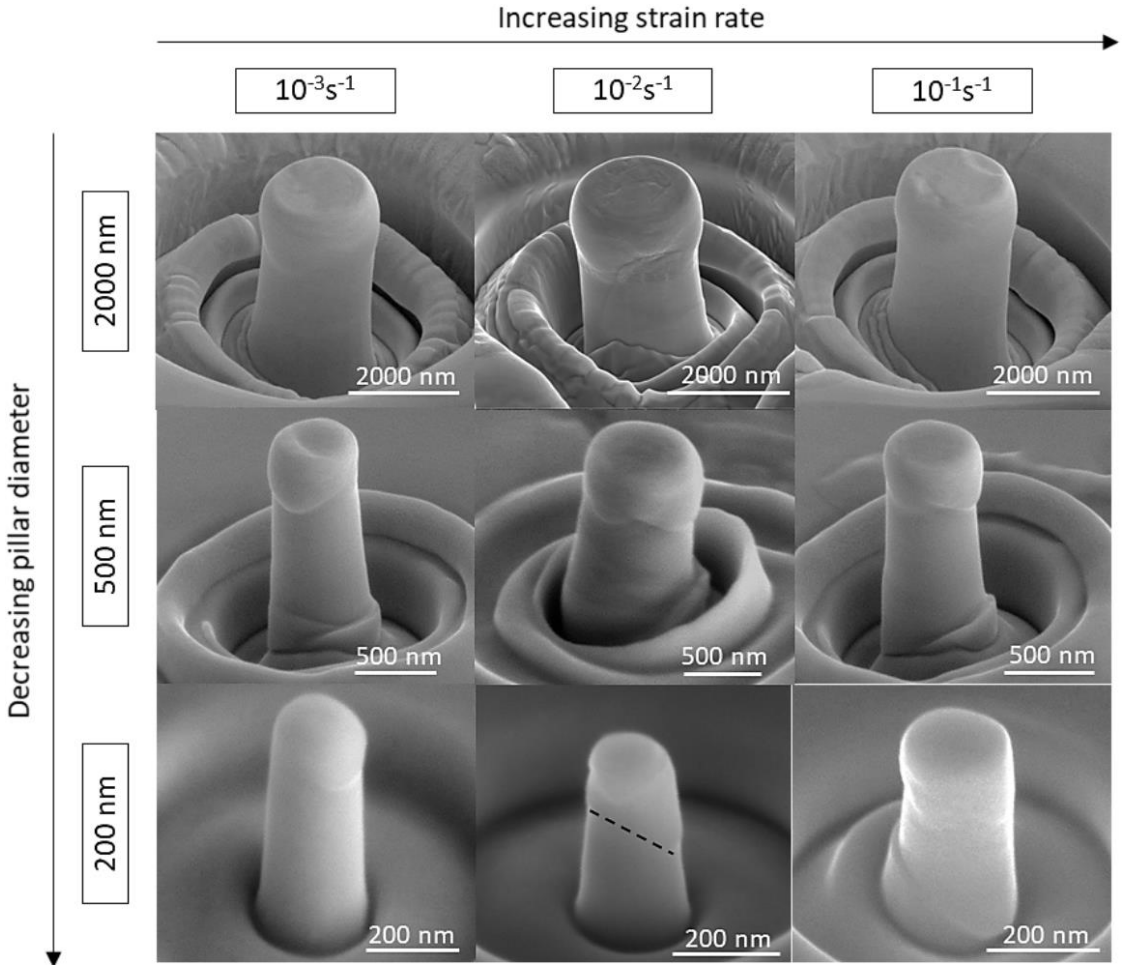

Figure 15. SEM images of post-compression W pillars.

While 2000 nm pillars show barreling and other multiple slip (homogenous) deformation across all strain rates, 500 nm and 200 nm pillars begin displaying quasi-single slip (localized) deformation at low strain rate, consistent with recent dislocation dynamics results [20] and observations in single crystal copper pillars [24], [25] attributed to the dislocation sources available to be activated. For 2000 nm and high strain rate 500 nm and 200 nm pillars, the deformation morphology is dominated by screw dislocation behavior over non-screw components. The cross-slip of screw dislocations and jog multiplication lead to frequent dislocation multiplication before surface annihilation, resulting in homogeneous deformation. However, for 500 and 200 nm pillars

at lower strain rates, the rapid glide of non-screw mixed dislocations is the dominating factor. As a result, these small sizes promote surface annihilation and suppress strong dislocation-dislocation interactions, so the deformation is mainly localized in the available activated dislocation sources [20]. As mentioned in Section 4.1, tapered pillars experience higher applied stress near their free end, thereby limiting even further the overall activated dislocation sources and deforming volume. As expected, regardless of it being homogenous or localized, deformation is focused on the upper portion of the pillar.

5 Conclusions

In-situ compression was performed at room temperature on cylindrical pillars of single crystal tungsten varying from 100 nm to 2000 nm in size at three strain rates (10^{-3} – 10^{-1} s^{-1}). The size effect and its influence on strain rate dependent factors of flow stress and strain hardening rate are analyzed qualitatively and quantitatively. Additional influence of size and strain rate on strain burst events as well as deformation morphology are described. The critical size for transition of all strain rate dependent properties appears around d < 500 nm.

The competition of size effect and strain rate effect on flow stress was evaluated two ways. The strain rate sensitivity, m, of flow stress was shown to decrease with decreasing pillar size, with 100 nm pillars even showing negative strain rate sensitivity at 8% flow stress. Accordingly, the size effect exponent, α, indicative of the strength of the size effect, was found to decrease with increasing applied strain rate. The change of strain rate sensitivity was explained through a transition from lattice friction dominated to dislocation bowout dominated flow stress, or through the change in overall dislocation mobility at small pillar diameter. This change in regime is also evident through the slope of strain bursts increasing with decreasing pillar diameter.

Strain hardening rate demonstrated clear size dependence and statistically insignificant strain rate dependence. While size dependence is attributed to the exhaustion of dislocation sources at small size, the strain rate dependence and scatter is explained through larger strain rate having larger strain burst magnitude.

Micron scale pillars have homogenous, bulk-like, plastic deformation over all strain rates, whereas nanoscale pillars demonstrate strain rate dependence with homogenous deformation at higher strain rate and localized plastic deformation at low strain rate due to limited availability of activated dislocation sources. The change in strain burst event appearance on the stress-strain curve from smooth to distinct strain burst and stress drop sections as pillar diameter decreases or at higher strain reflects this.

While this thesis attempts to give a complete picture of the size effect on strain rate influenced flow behavior of single crystal tungsten, there remains much to be determined. As an important material property, investigation is currently underway on the fracture toughness of single crystal tungsten beams at micron and nanoscale cross-sectional sizes and various strain rates. Additional experimentation is also being carried out for ultra-high strain rate data, both through possible step loading of the PI 85 or through *ex situ* impact testing. The analogy of increasing strain rate to decreasing temperature as well as the real time dislocation structure of the compressed pillar are also of interest.

References

[1] Dümmer, T., Lasalvia, J., Ravichandran, G., & Meyers, M. Effect of strain rate on plastic flow and failure in polycrystalline tungsten. *Acta Mater.* **46(17**), 6267–6290 (1998).

[2] Gröger, R., Bailey, A., & Vitek, V. Multiscale modeling of plastic deformation of molybdenum and tungsten: I. Atomistic studies of the core structure and glide of 1/2〈111〉 screw dislocations at 0 K. *Acta Mater.* **56(19),** 5401–5411 (2008).

[3] Uchic, M. D., Shade, P. A., & Dimiduk, D. M. Plasticity of micrometer-scale single crystals in compression. *Annu. Rev. Mater. Res.* **39,** 361–386 (2009).

[4] Kim, J.-Y., Jang, D., & Greer, J. R. Tensile and compressive behavior of tungsten, molybdenum, tantalum and niobium at the nanoscale. *Acta Mater.* **58(7),** 2355–2363 (2010).

[5] Zaiser, M. Schwerdtfeger, J., Schneider, A., Frick, C., Clark, B.G., Gruber, P. & Arzt, E. Strain bursts in plastically deforming molybdenum micro-and nanopillars. *Philos. Mag.* **88(3032)** 3861–3874 (2008).

[6] Marichal, C. Srivastava, K., Weygand, D., Van Petegem, S., Grolimund, D., Gumbsch, P. & Van Swygenhoven, H. Origin of anomalous slip in tungsten. *Phys. Rev. Lett.* **113(2),** 025501 (2014).

[7] Huang, L. Li, Q.-J., Shan, Z.-W., Li, J., Sun, J., & Ma, E. A new regime for mechanical annealing and strong sample-size strengthening in body centered cubic molybdenum. *Nat. Commun.* **2,** 547 (2011).

[8] Nix, W. D. & Cai, W. Plasticity of BCC micropillars controlled by competition between dislocation multiplication and depletion. *Acta Mater.* **61(9),** 3233–3241 (2013).

[9] Kaufmann, D., Schneider, A., Mönig, R., Volkert, C. & Kraft, O. Effect of surface orientation on the plasticity of small BCC metals. *Int. J. Plasticity* **49,** 145–151 (2013).

[10] Deutges, M., Knorr, I., Borchers, C., Volkert, C. A., & Kirchheim, R. Influence of hydrogen on the deformation morphology of vanadium (100) micropillars in the α-phase of the vanadium–hydrogen system. *Scripta Mater.* **68(1),** 71–74 (2013).

[11] Cui, Y. Po, G., & Ghoniem, N. Temperature-insensitivity of the flow stress in body-centered cubic micropillar crystals. *Acta Mater.* **108,** 128–137 (2016).

[12] Huang, R. Li, Q.-J., Wang, Z.-J., Huang, L., Li, J., Ma, E., & Shan, Z.-W. Flow stress in submicron bcc iron single crystals: sample-size-dependent strain-rate sensitivity and rate-dependent size strengthening. *Mater. Res. Lett.* **3(3),** 121–127 (2015).

[13] Jia D., Ramesh K. T., & Ma E. Effects of nanocrystalline and ultrafine grain sizes on constitutive behavior and shear bands in iron. *Acta Mater.* **51(12),** 3495–3509 (2003).

[14] Cheng, G. M., Jian, W. W., Xu, W. Z., Yuan, H., Millet, P. C., & Zhu, Y. T. Grain size effect on deformation mechanisms of Nanocrystalline bcc metals. *Mater. Res. Lett.* **1(1),** 26–31 (2013).

[15] Wei, Q., Cheng, S., Ramesh, K. T., & Ma, E. Effect of nanocrystalline and ultrafine grain sizes on the strain rate sensitivity and activation volume: fcc versus bcc metals. *Mater. Sci. Eng. A.* **381(1–2),** 71–79 (2004).

[16] Wei, Q. Jiao, T., Ramesh, K. T., Ma, E., Kecskes, L. J., Magness, L., Dowding, R., Kazykhanov, V. U., & Valiev, R. Z. Mechanical behavior and dynamic failure of high-strength ultrafine grained tungsten under uniaxial compression. *Acta Mater.* **54(1),** 77–87 (2006).

[17] Wei, Q., Pan, Z. L., Wu, X. L., Schuster, B. E., Kecskes, L. J., & Valiev, R. Z. Microstructure and mechanical properties at different length scales and strain rates of nanocrystalline tantalum produced by high-pressure torsion. *Acta Mater*. **59(6),** 2423–2436 (2011).

[18] Schneider, A. S., Clark, B. G., Frick, C. P., Gruber, P. A., & Arzt, E. Effect of orientation and loading rate on compression behavior of small-scale Mo pillars. *Mater. Sci. Eng. A.* **508(1–2),** 241-246 (2009).

[19] Semiatin, S. L. & Altan, T. Measurement and interpretation of flow stress data for the simulation of metal-forming processes. In *ASM Handbook* (eds Furrer, D. U. & Semiatin, S. L.) Vol. 22B *Metals Process Simulation*, 46–66 (ASM International, 2010).

[20] Cui, Y. Po, G., Srivastava, P., Jiang, K., Gupta, V., Ghoniem, N. The role of slow screw dislocations in controlling fast strain avalanche dynamics in body-centered cubic metals. In press. *Int. J. Plasticity* (2019).

[21] Pozuelo, M., Stremfel, J. W., Yang, J.-M., & Marian, J. Strengthening to softening transition in lath martensite. *Materialia* **5(10),** 100254 (2019).

[22] Ni, X., Papanikolaou, S., Vajente, G., Adhikari, R. X., & Greer, J. R. Probing microplasticity in small-scale FCC crystals via dynamic mechanical analysis. *Phys. Rev. Lett.* **118(15),** 155501 (2017).

[23] Abad, O. T., Wheeler, J. M., Michler, J., & Schneider, A. S. Temperature-dependent size effects on the strength of Ta and W micropillars. *Acta Mater.* **103,** 483–494 (2016).

[24] Kiener, D. & Minor, A. M. Source-controlled yield and hardening of Cu(1 0 0) studied by in situ transmission electron microscopy. *Acta Mater.* **59(4),** 1328–1337 (2011).

[25] Zhang, J. Y., Liang, X, Zhang, P., Wu, K., Liu, G., & Sun, J. Emergence of external size effects in the bulk-scale polycrystal to small-scale single-crystal transition: A maximum in the strength and strain-rate sensitivity of multicrystalline Cu micropillars. *Acta Mater.* **66,** 302–316 (2014).

[26] Shan, Z. W., Mishra, R. K., Syed Asif, S. A., Warren, O. L., & Minor, A. M. Mechanical annealing and source-limited deformation in submicrometre-diameter Ni crystals. *Nat. Mater.* **7,** 115–119 (2008).

[27] Alturk, R., Mates, S., Xu, Z., & Abu-Farha, F. Effects of microstructure on the strain rate sensitivity of advanced steels. In (eds TMS T.) *TMS 2017 146th Annual Meeting & Exhibition Supplemental Proceedings*. *The Minerals, Metals & Materials Series* (Springer, Cham, 2017).

[28] Volkert, C. A., & Lilleodden, E. T. Size effects in the deformation of sub-micron Au columns. *Philos. Mag.* **86(33–35),** 5567–5579 (2006).

[29] Schneider, A. S., Frick, C. P., Clark, B. G., Gruber, P. A., & Arzt, E. Influence of orientation on the size effect in bcc pillars with different critical temperatures. *Mater. Sci. Eng. A* **528(3),** 1540–1547 (2011).